Supporting Information -

Temperature-Responsive Nanomagnetic Logic

Gates for Cellular Hyperthermia

Rui Oliveira-Silva,[†,‡] Rute A. Pereira,[†] Fábio M. Silva,[†] Vítor M. Gaspar,[¶]

Alfonso Ibarra,[§] Ángel Millán,[‖] Filipa L. Sousa,[¶] João F. Mano,[¶] and Nuno J.

O. Silva[*,†]

[†]*Departamento de Física and CICECO, Aveiro Institute of Nanotechnology Universidade de Aveiro, 3810-193 Aveiro, Portugal.*

[‡]*Univ. Lisbon, Inst. Super. Tecn., Inst. Bioengn. & Biosci., Dept. Bioengn., Ave Rovisco Pais, P-1049001 Lisbon, Portugal.*

[¶]*Departamento de Química and CICECO, Aveiro Institute of Nanotechnology, Universidade de Aveiro, 3810-193 Aveiro, Portugal.*

[§]*LMA, Instituto de Nanociencia de Aragón, Universidad de Zaragoza.*

[‖]*Instituto de Ciencia de Materiales de Aragón, CSIC - Universidad de Zaragoza. Departamento de Física de la Materia Condensada, Facultad de Ciencias, 50009 Zaragoza, Spain.*

E-mail: nunojoao@ua.pt

Detailed experimental description

Here we detail the synthesis and experiments performed in four samples of Fe_3Se_4 nanoplatelets, whose general procedure is given in the manuscript. Specific conditions and selected prop-

erties are given in table 1.

Synthesis of precursors

Fe-oleate was prepared and washed using standard procedures .[1] Washing processes included an extraction with a mixture of ethanol acetone and a redispersion with hexane followed by an evaporation step at room temperature. These steps were repeated form 2 to 4 times, resulting in brown Fe-oleates spanning from a slightly viscous behaviour to a solid darker wax, used to produce smaller and larger nanoplatelets, respectively. The Se-octadecene complex was also prepared using standard procedures[2] by the reaction of 434 mg of metallic Se powder with 75.3 g of 1-octadecene during 30 min at 180 °C.

Microscopy

Transmission electron microscopy (TEM) on the nanoparticles was performed using a Hitachi H9000 microscope, working at 300 kV. Scanning Transmission Electron Microscopy - High Angle Annular Dark Field (STEM-HAADF) images were obtained in a probe-corrected Titan (FEI) at a working voltage of 300 kV, coupled with a HAADF detector (Fischione). In order to analyse the chemical composition of the materials, X-ray Energy Dispersive Spectra (EDS) were obtained with an EDAX detector. Samples for TEM observations of the NPs dispersed in the ferrofluids were prepared by dip coating of carbon coated copper grids.

Prostate cancer cells were washed 3 times with PBS and imaged in a Zeiss Imager M2 fluorescence microscope (Carl Zeiss Microscopy GmbH, Germany), equipped with a 10x/0.25 Plan Apochromat air objective. All the data was processed in the Zeiss Zen software (v 2.3).

X-ray diffraction

X-ray diffraction (XRD) measurements were performed at room temperature with a PANalytical Empyrean powder diffractometer using monochromated CuK_α radiation ($\lambda = 1.541$

Å) in the 10 - 80° 2θ range at 0.02° resolution, and 4000 acquisition points per step. The incident beam optics included a Soller slit of 0.04 rad, a 10 mm fixed mask, a divergence fixed slit of 1/4 and an anti-scatter slit of 1/8. The diffracted beam optics included a Soller slit of 0.04 rad and anti-scatter slit of 7.5 mm. The analysis of the diffraction patterns was performed by Rietveld refinement using the $FullProf$ package.[3] The size effects were treated with the integral breadth method using the Voigt model for both the instrumental and intrinsic diffraction peak shape considering a Thompson-Cox-Hastings pseudo-Voigt convoluted with Axial divergence asymmetry function to describe the peak shape. The contribution of the instrument to the peaks broadening was determined by the refinement of the XRD pattern of a LaB_6 standard sample (NIST ref. 660a).

Magnetic data

Magnetic measurements were performed in a superconducting quantum interference device (SQUID) magnetometeres model MPMS-XL and MPMS3, from Quantum Design Inc, under helium atmosphere and under controlled magnetic field and temperature. The field is provided by a superconducting magnet and temperature is controlled in feedback using a cold helium flow and a heater acting on the flow

X-ray photoelectron spectroscopy

The X-ray photoelectron spectroscopy (XPS) analysis was carried out using a Kratos Axis SUPRA spectrometer employing a monochromatic Al K_α (1486.6 eV) 15 mA, 15 kV) X-ray source and a power of 225 W.

Cell culture

Prostate cancer cells (PC-3) were routinely cultured in RPMI-1640 medium supplemented with 10% FBS and 1% antibiotic/antimycotic. PC-3 cells were grown in cell culture treated t-

flasks in a temperature-controlled incubator at 37°, 5% CO_2 and in a humidified atmosphere. Upon reaching confluency cells were detached by using TripLE™Xpress and subcultured.

Hyperthermia studies on cells

The normal use of the nanoplatelets as logic gates, to know if a temperature threshold during irradiation is crossed, involves setting them in a high magnetization state (M=1) by the application of a (high) magnetic field (H=1), followed by the irradiation procedure and followed by measuring the final magnetization state, which may or may not have changed to zero due to irradiation). Although less useful in practice, the use of the SR latch gate can be reversed and used to detect any magnetic field going above a threshold during a period of time where temperature is known to be always below T_C. In this case, temperature is turned first such that magnetization is reset low (M=0) and any possible field during a given period of time will set magnetization in a high state (Q=1).

Simulations

Thermal simulations were performed using the finite element analysis software QuickField™Professional 6.3. We considered a axial symmetric geometry with hot spots representing the nanoplatelets at a constant temperature (42 °C) embedded in a 780 µm thick Matrigel™layer with thermal conductivity 0.5 W/Km and a 20 µm thick cell layer with the same conductivity. The top cell layer exchanges heat with the cell medium by convection, simulated using a surface convection boundary condition with $h = 500$ W/Km^2 and ambient temperature 37 °C.[4] The remaining Matrigel™and cell surfaces exchange heat by conduction with a plastic frame (thermal conductivity 0.4 W/Km), which in turn exchanges heat with air by convection ($h = 10$ W/Km^2 and ambient temperature 37 °C). This simulation provides an estimation of the maximum expected temperature difference between the nanoplatelets and the cells due to the chosen geometry. Additional temperature drops may occur at the micro/nano interfaces and are presently a matter of debate (see, for instance, Ref.[5]). Such additional

temperature drops would be present even if the nanoplatelets were mixed together will cells.

References

(1) L. M. Bronstein, X. Huang, J. Retrum, A. Schmucker, Maren Pink, Barry D. Stein, and Bogdan Dragnea. Influence of iron oleate complex structure on iron oxide nanoparticle formation. *Chem. Mater.*, 19:3624–3632, 2007.

(2) Craig Bullen, Joel van Embden, Jacek Jasieniak, Joanna E. Cosgriff, Roger J. Mulder, Ezio Rizzardo, Min Gu, and Colin L. Raston. High activity phosphine-free selenium precursor solution for semiconductor nanocrystal growth. *Chemistry of Materials*, 22(14):4135–4143, 2010.

(3) J. Rodríguez-Carvajal. *Physica B*, 192:55, 1993.

(4) Sean D. Lubner, Jeunghwan Choi, Geoff Wehmeyer, Bastian Waag, Vivek Mishra, Harishankar Natesan, John C. Bischof, and Chris Dames. Reusable bi-directional 3 sensor to measure thermal conductivity of 100-m thick biological tissues *Review of Scientific Instruments*, 86:014905, 2015.

(5) G. Baffou, H. Rigneault, D. Marguet, L. Jullien. A critique of methods for temperature imaging in single cells. *Nat. Methods*, 11(9):899-901, 2014.

Tables and figures

Table 1: Relevant parameters of synthesis conditions, morphology and magnetic properties of the four samples of Fe_3Se_4 nanoplatelets presented in the manuscript. The diameter of the nanoplatelets is estimated as the distance across two parallel edges. D_g is calculated using the average diameter and thickness considering that the nanoplatelets are flat cylinders.

synthesis conditions			characteristic sizes and magnetic phase transition				
ramp rate ($°C/min$)	T_{max} ($°C$)	time @T_{max} (h)	diameter (nm)	thickness (nm)	XRD size (nm)	D_g (nm)	T_C ($°C$)
7.5	210	1	130	43	18	95	18
5	210	1	95	36	26	70	36
18	210	0.75	193	46	21	137	22
18	210	1	250	60	31	180	42

Table 2: True table of the SR latch as usually presented, showing the output of the logic circuit at a time t ($Q(t)$), the subsequent action on S, R, or both and the resulting output at a time $t+1$ ($Q(t+1)$). RC stands for 'race condition', where the state $Q(t+1)$ is ill-defined and depend on which S or R is set low in first place. In the present case, Q corresponds to the magnetization M, S corresponds to the field H and R corresponds to temperature T.

$Q(t)$	S	R	$Q(t+1)$
0	0	0	0
0	0	1	0
0	1	0	1
0	1	1	RC
1	1	1	RC
1	0	0	1
1	0	1	0
1	1	0	1
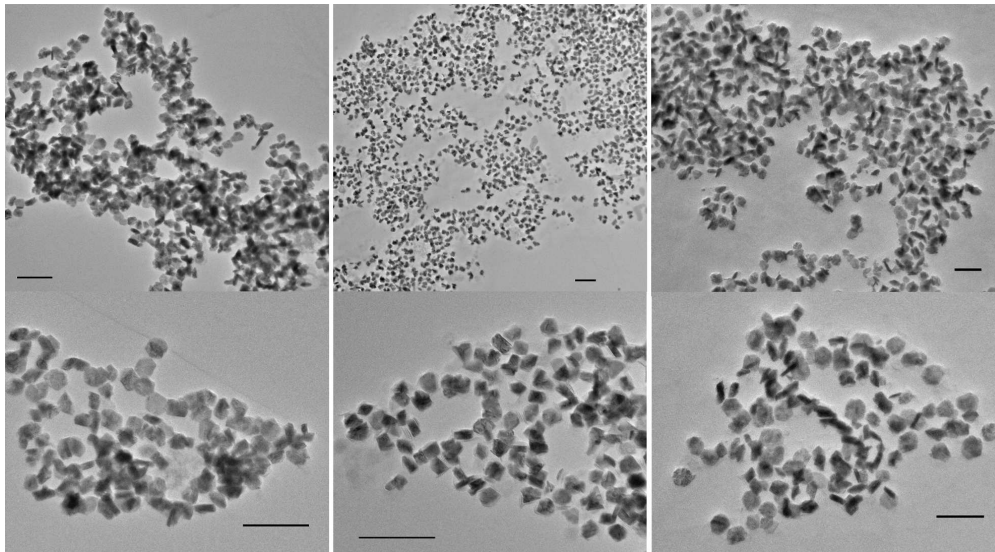
Figure 1: **Electron microscope images of Fe$_3$Se$_4$ nanoplatelets.** Left column shows images of sample with average lateral diameters of 130 nm, central column 95 nm and right column 193 nm. All scale bars correspond to 500 nm.
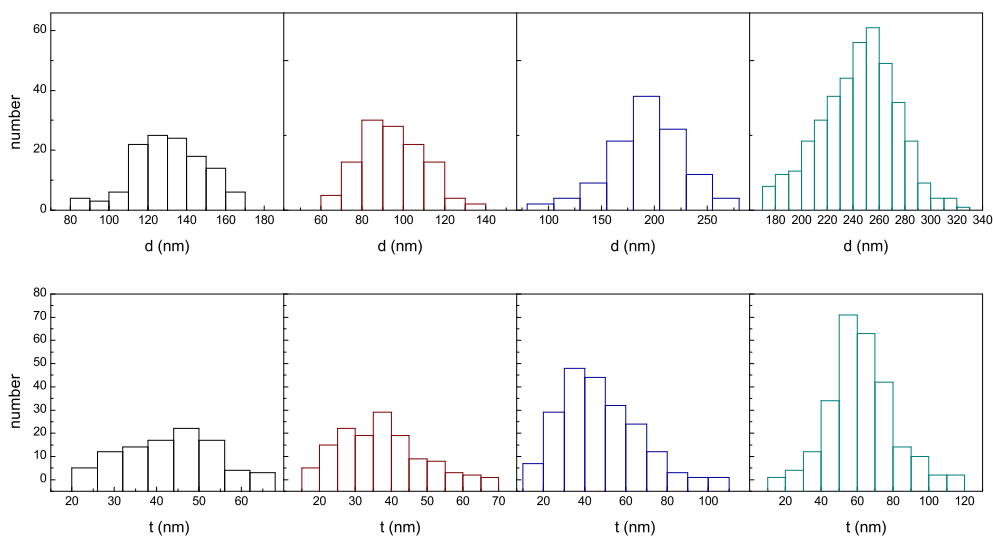
Figure 2: **Diameter and thickness distributions of the Fe$_3$Se$_4$ nanoplatelets.**
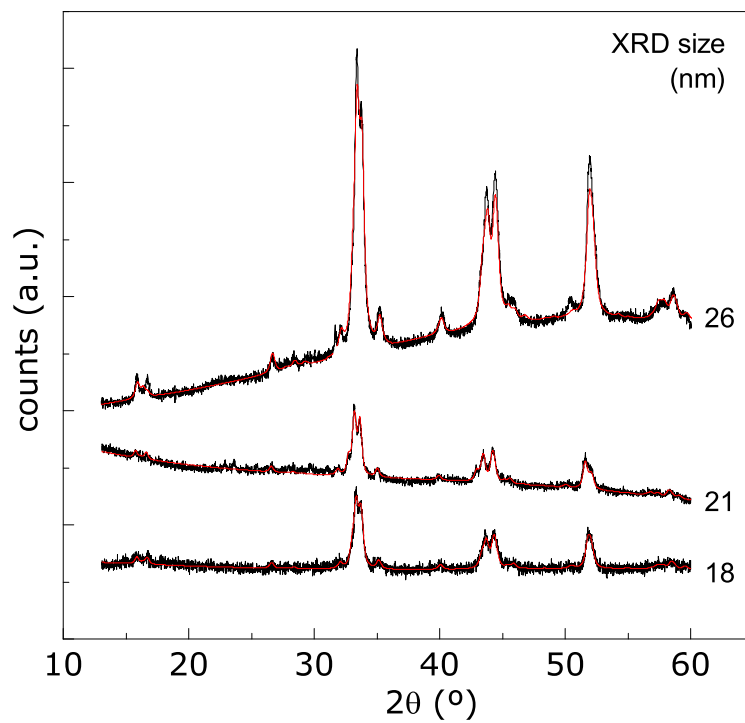
Figure 3: **X-ray diffraction patterns of Fe$_3$Se$_4$ nanoplatelets.** Continuous (red) line represents Rietveld refinement to the XRD data. Average apparent sizes are shown in the right side of the plot.
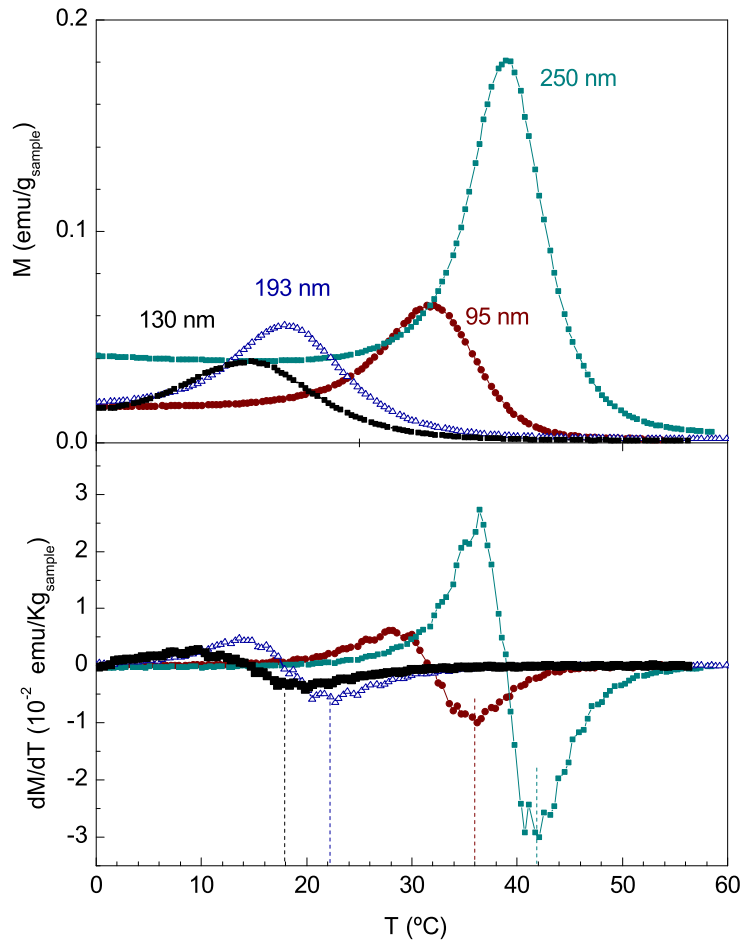
Figure 4: **Magnetization of Fe₃Se₄ nanoplatelets with different average lateral diameter as a function of temperature and associated derivative.** T_C is taken as the minimum of that derivative, i. e., the inflexion point of the M(T) data.
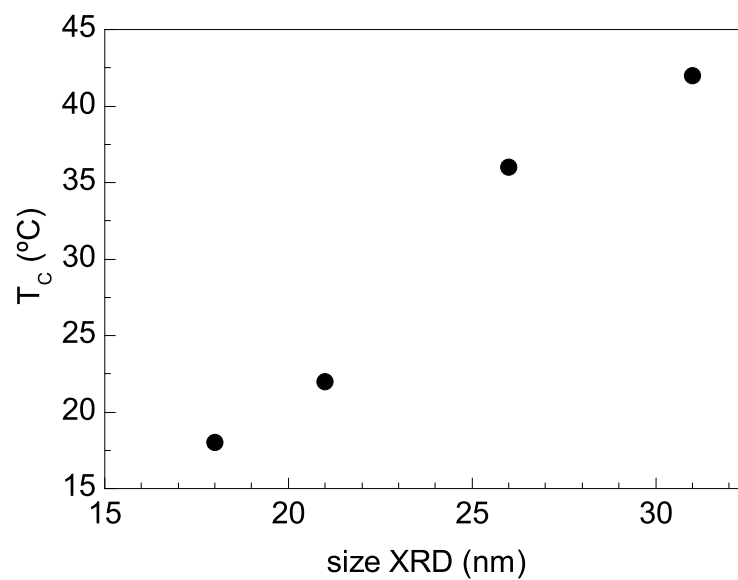
Figure 5: **Average apparent sizes obtained from Rietveld refinement as a function of the transition temperature** T_C.
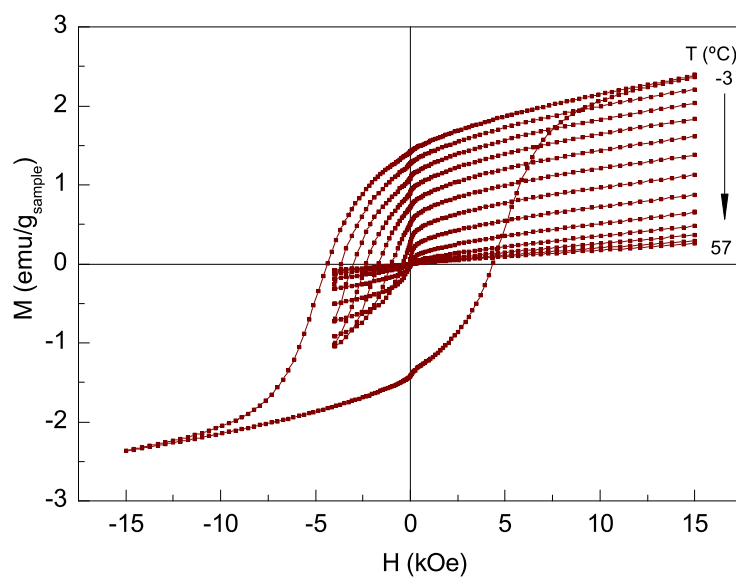
Figure 6: **Dependence of magnetization with the external magnetic field.** Curves were recorded at selected temperatures around room temperature in the Fe_3Se_4 nanoplatelets with an average diameter of 95 nm.
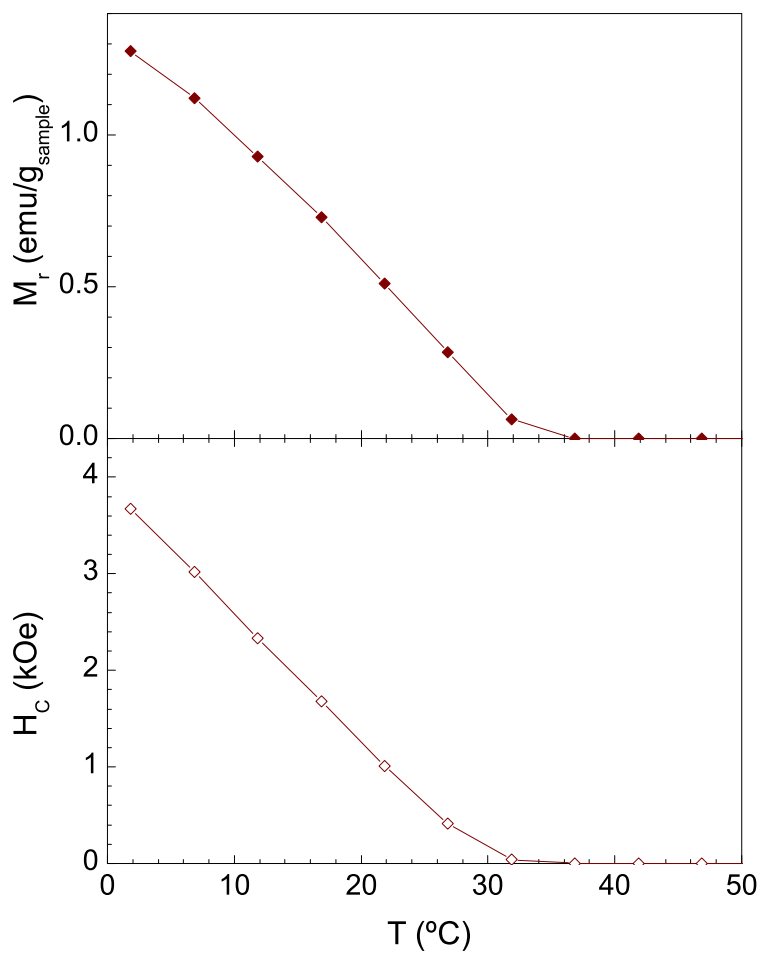
Figure 7: **Remanent magnetization, susceptibility and coercive field of the Fe$_3$Se$_4$ nanoplatelets with average diameter/thickness of 95 nm.** All data shown was taken from the hysteresis cycles shown in the previous figure.
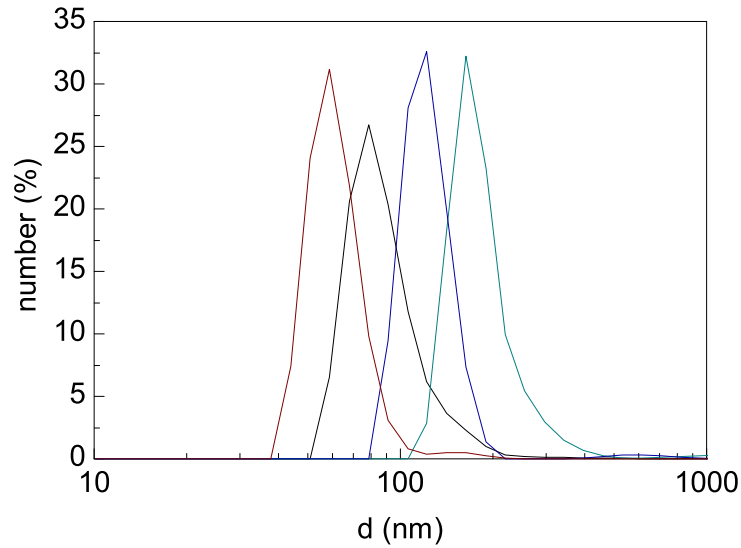
Figure 8: **Diameter size distributions of the colloidal suspensions of the Fe$_3$Se$_4$ nanoplatelets.** Hydrodynamic size distribution obtained with dynamic light scattering. The average hydrodynamic sizes are compatible with suspensions of isolated Fe$_3$Se$_4$ nanoplatelets. In fact, these sizes are systematically smaller than the average diameter obtained from electron microscopy and close to the average gyration diameter (D_g) obtained for flat cylinders (gyration radius $R_g^2 = (a^2/2) + (t^2/12)$ where R_g is half of the gyration diameter, a is half of the average diameter and t is the thickness of the nanoplatelets).
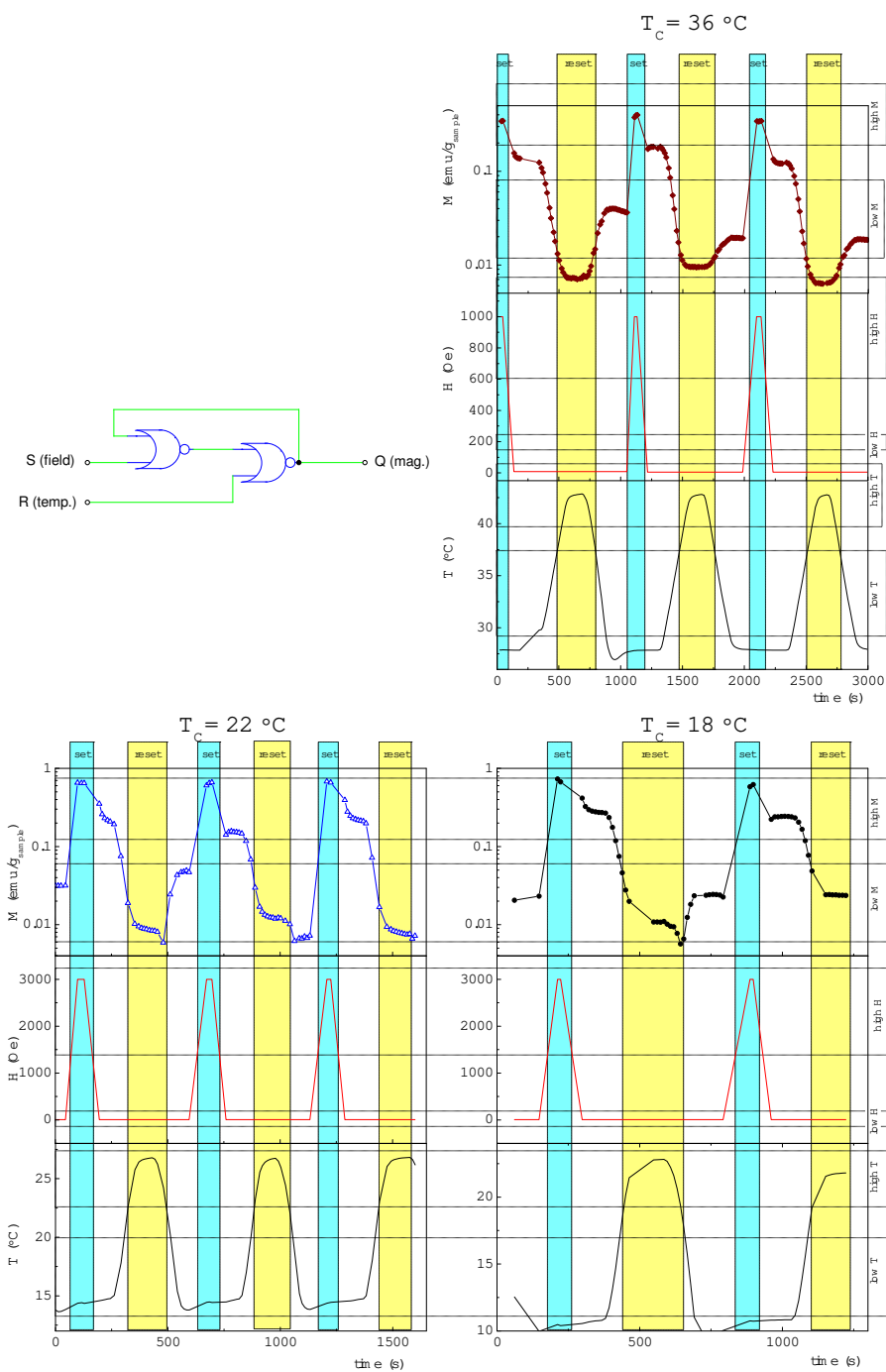
Figure 9: **Logic element representation of the bistable gate (SR latch) and examples of the time diagram of the gate.** The gate can be represented by two NOR elements in feedback, with two possible inputs, a set (S) and a reset (R), and one output (Q). Example of functioning of the logic gate as a function of time in samples with different T_C, showing the basic operations of the gate based on the response of magnetization (Q) to the field (S) and temperature (R) inputs.

13

Figure 10: **Simulated temperature distribution at equilibrium of the cell culture.** Estimation of the temperature distribution on the cell culture chambers containing the Matrigel^{TM}, nanoplatelets, cells and cell medium when the nanoplatelets are at 42 °C and the total heat flux generated by the nanoplatelets is 0.045 W across a 0.12 cm^2 surface. The layered system used in the cell hyperthermia experiments introduces *per se* a maximum temperature drop between nanoplatelets and cells of ~0.5 °C and any additional temperature drop will be due to intrinsically lower thermal conductivity at the micro and interfaces which would be present even in a non-layered geometry where cells and nanoplatelets were mixed without internalization.
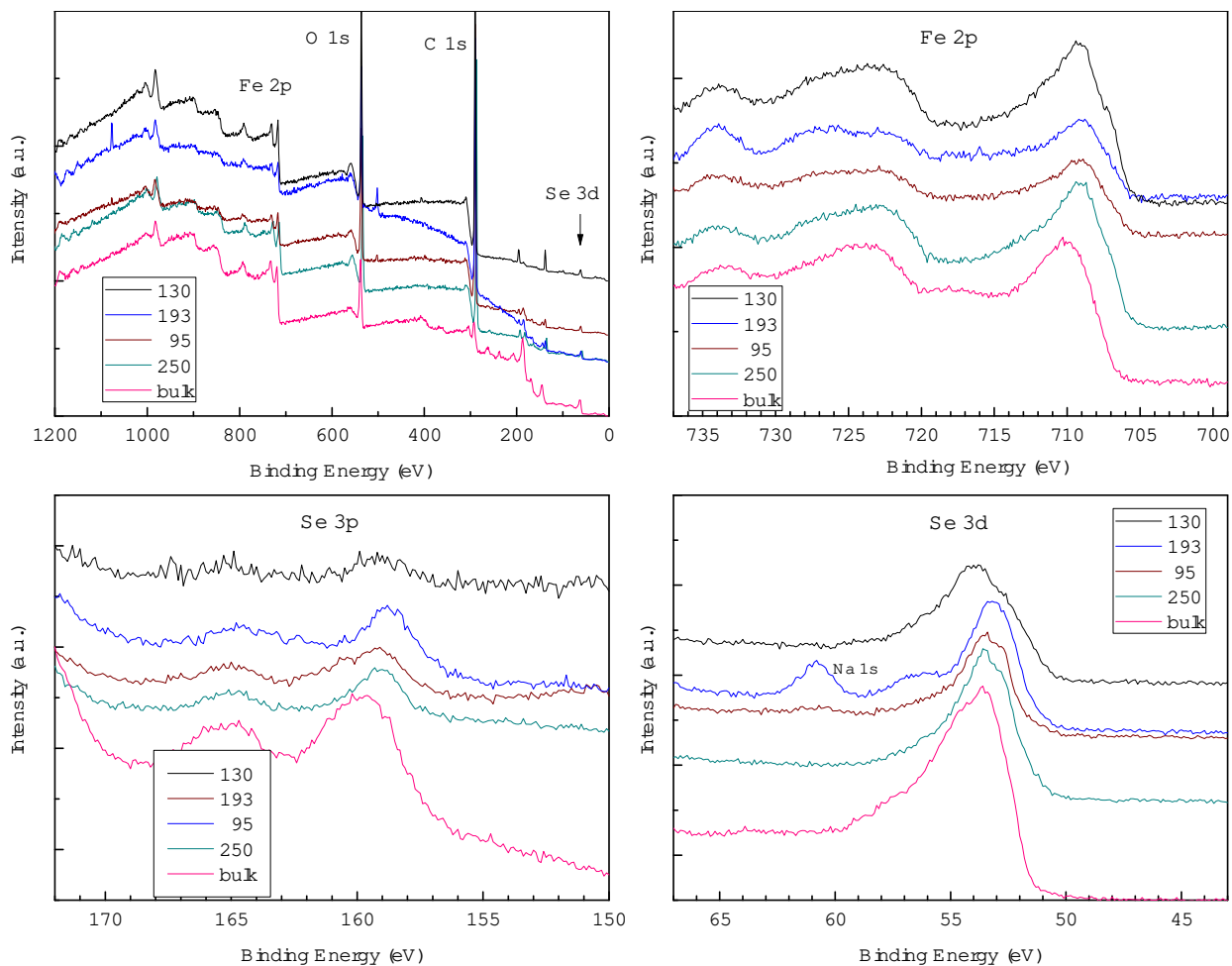
Figure 11: **XPS data of the Fe$_3$Se$_4$ nanoplatelets (with different average sizes) and reference (bulk) sample** The panels show the full spectra and the high resolution Fe 2p, Se 3p and Se 3d spectra. The spectra show small differences among the nanoplatelets with different average sizes and shifts to lower energy values when compared to the microcrystalline sample. This shift is of the order of the uncertain associated to the C 1s peak used to correct the effect of the charge neutralizer and therefore it can be an intrinsic effect (associated to different Fe and Se environments/oxidation states) or a spurious effect since the C 1s found in the nanoplatelets is probably different from that found in the microcrystalline sample. Apart this shift, the most noticeable difference between spectra is a satellite peak near 717.6 eV found only in the microcrystalline sample and the broadening/deconvolution around the 725 eV region. One of the samples shows a contamination with Na.

15
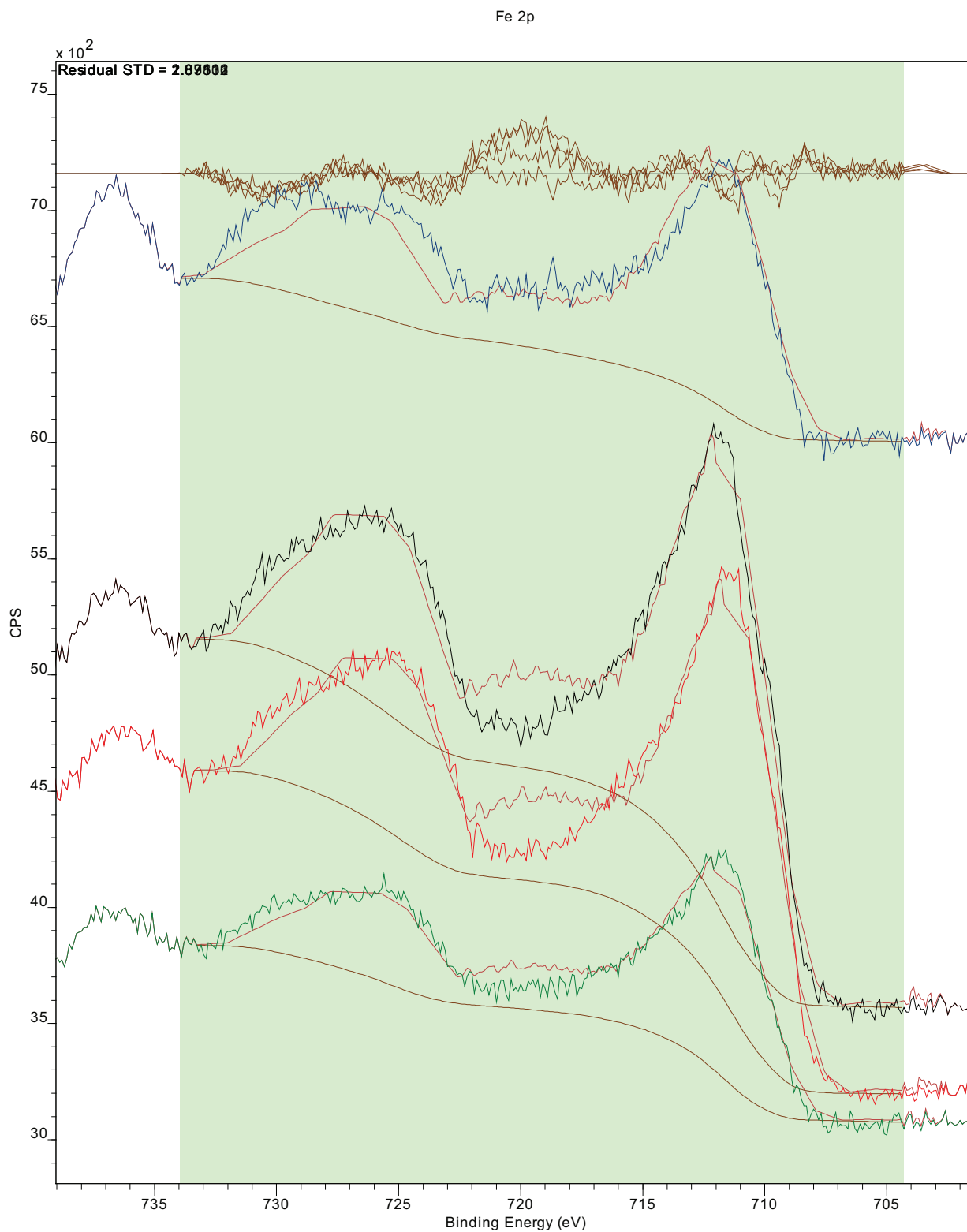
Figure 12: High resolution XPS Fe 2p spectra of the nanoplatelets fitted to that of the microcrystalline sample, allowing an energy shift.

16
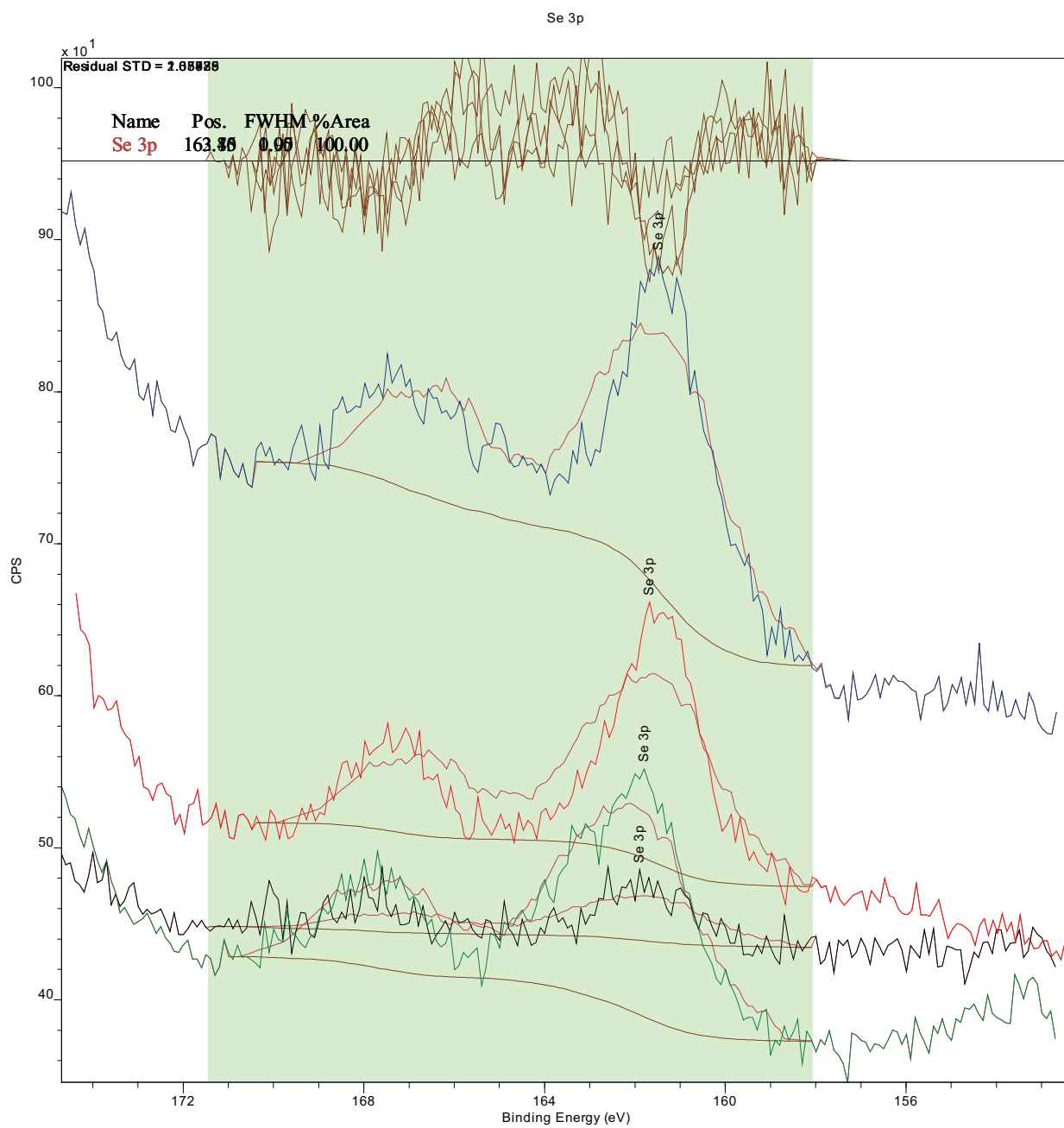
Figure 13: High resolution XPS Se 3p spectra of the nanoplatelets fitted to that of the microcrystalline sample, allowing an energy shift.
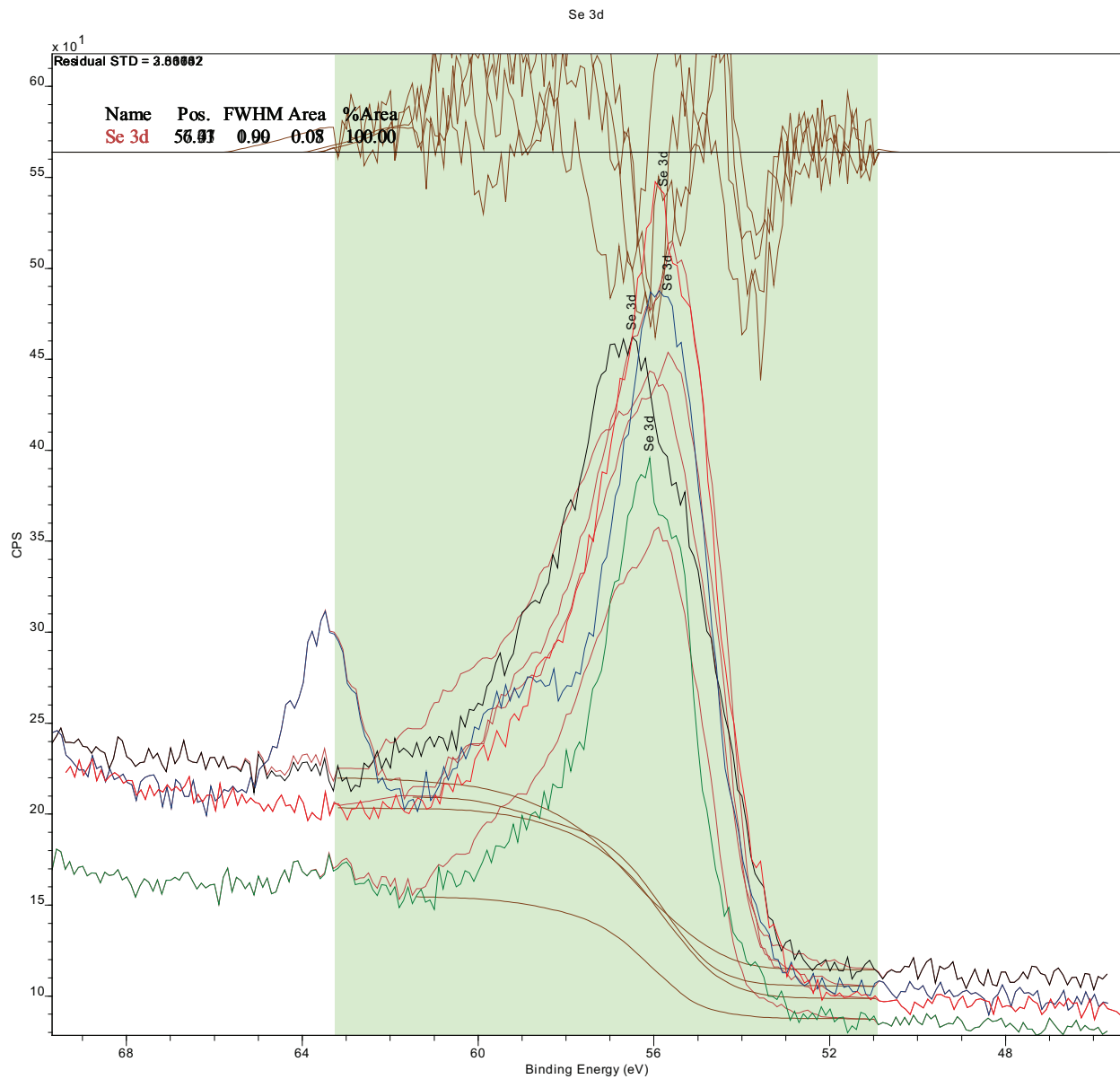
Figure 14: High resolution XPS Se 3d spectra of the nanoplatelets fitted to that of the microcrystalline sample, allowing an energy shift.
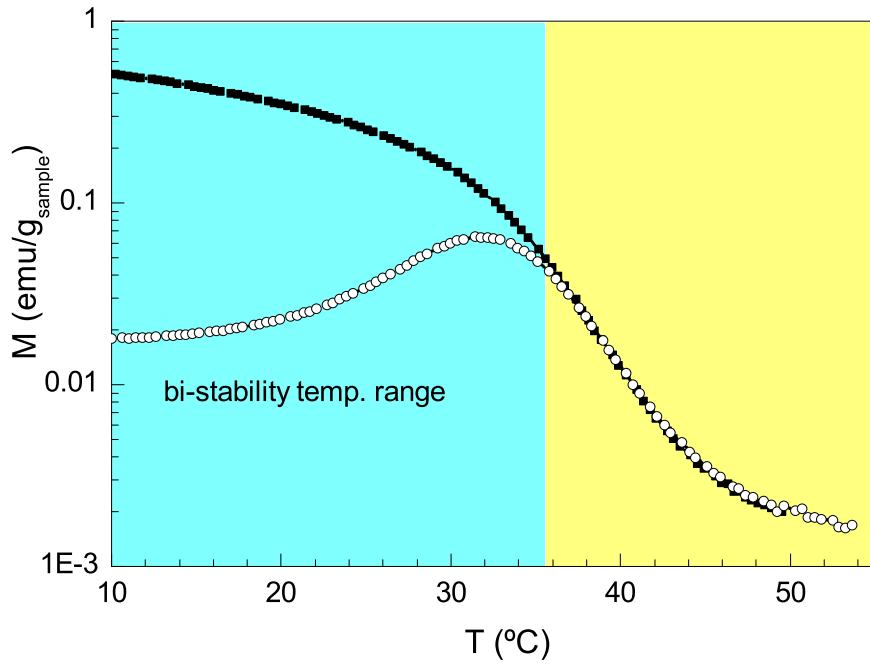
Figure 15: **Standard zero-field cooling (ZFC) and field cooling curves (FC).** Magnetization was recorded as a function of temperature around room temperature at a low applied field (H_{app} = 50 Oe) after cooling from 60 °C under zero field (ZFC, open circles) and after cooling under H_{app} (FC, filled squares). Data was recorded on Fe_3Se_4 nanoplatelets with average diameter of 95 nm. Below ~ 35 °C the curves diverge and the system can be in a high or a low state. Above that temperature the system can be reset.
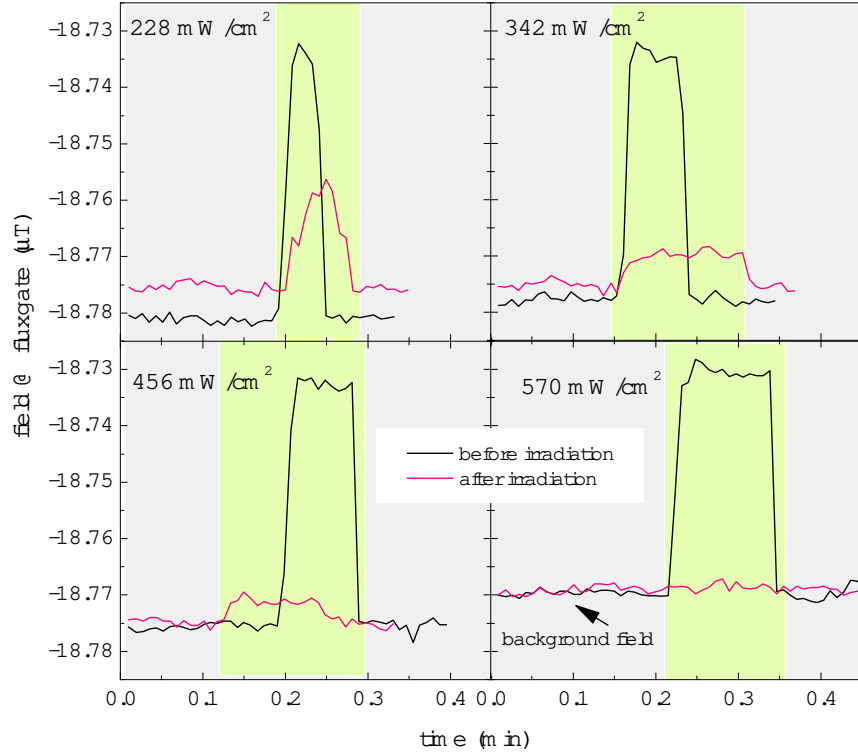
Figure 16: **Remanent magnetization M_r measured by the fluxgate magnetometer on the cell wells before and after irradiation with a given power during 5 minutes.** The nanoplatelets were set in a *high* state *before* irradiation and then approached to the fluxgate magnetometer that senses an increase of magnetic field of the order of $0.05\,\mu T$ due to dipolar magnetic field created by the M_r of the nanoplatelets (black curves). The curves show the ambient background field (grey areas) and the field created by the nanoplatelets plus background (green areas). After irradiation, the nanoplatelets were again approached to the fluxgate to measure again the dipolar magnetic field (red curves, green area); this field decreases as the power increases, vanishing into the background noise for a power between 456 and 570 mW/cm^2.
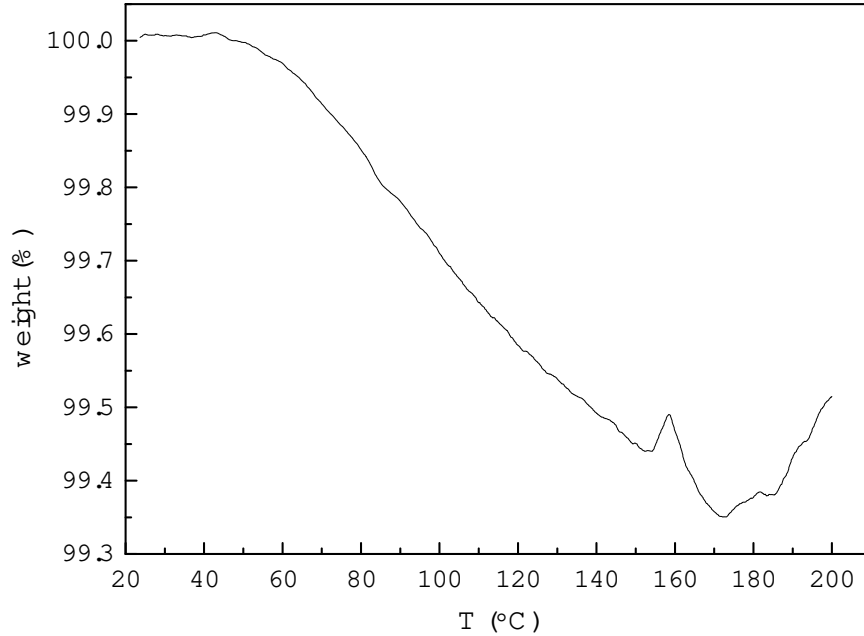
Figure 17: **Thermogravimetric analysis on the Fe$_3$Se$_4$ nanoplatelets before phase transfer.** Analysis was performed on a Shimadzu TGA-50 thermogravimetric analyser, using a heating rate of 5 °C/min under air atmosphere, with a flow rate of 20 mL/min. The sample holder was a 5 mm diameter platinum plate and the sample mass was 4.03 mg.
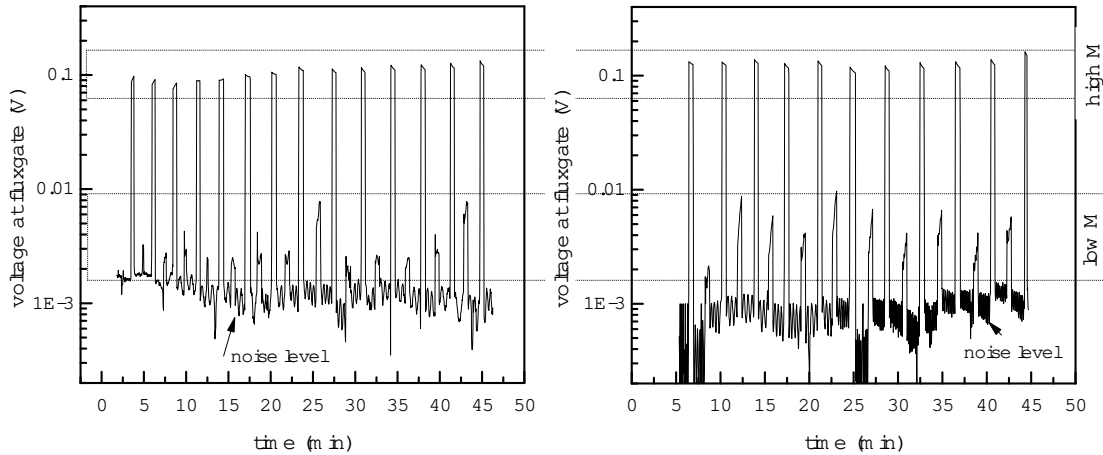
Figure 18: **Reproducibility tests.** Repetition of set/reset cycles measuring the output voltage at the fluxgate magnetometer induced by the high and low magnetization states of the logic gates. The high and low states are clearly separated by an order of magnitude of signal difference. The oscillations from cycle to cycle are much smaller than this difference. We present 2 groups of measurements performed on different days.
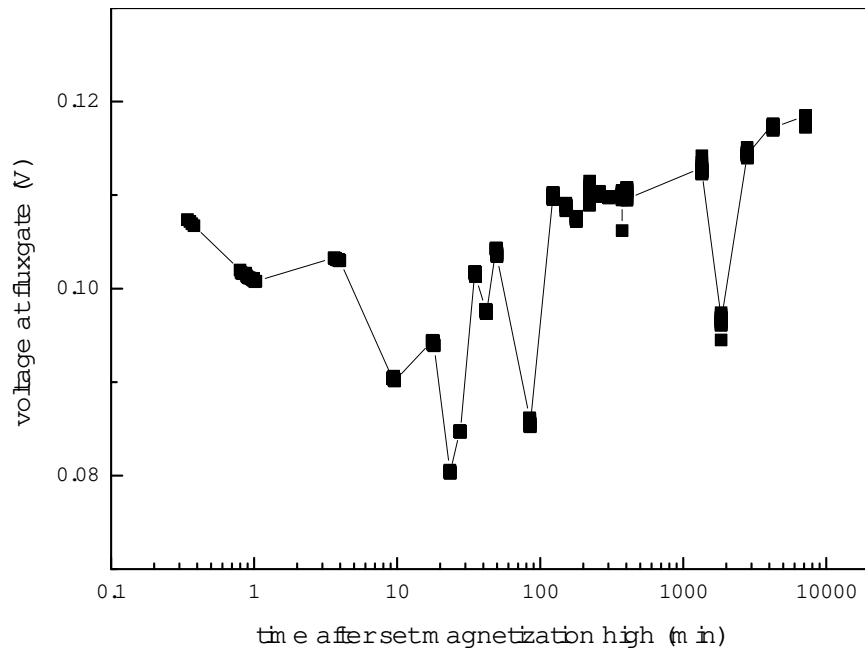
Figure 19: **Stability tests.** Stability over time of the output voltage at the fluxgate magnetometer after setting magnetization in the high state. The fluctuation of the response is quite low compared to the difference between the high and low magnetization levels. A long stability means that the logic gates can test a possible temperature threshold surpass occurring in a wide time frame.